Frustrated and Allowed Structural Transitions: The Theory-Guided Discovery of the Modulated Structure of IrSi

Hillary E. Mitchell Warden and Daniel C. Fredrickson*

Department of Chemistry, University of Wisconsin-Madison, 1101 University Avenue, Madison, Wisconsin 53706, United States

ABSTRACT: To the experienced molecular chemist, predicting the geometries and reactivities of a system is an exercise in balancing simple concepts, such as sterics and electronics. In this Article, we illustrate how recent theoretical developments can give this combination of concepts a similar predictive power in intermetallic chemistry, through the anticipation and discovery of structural complexity in the nominally MnP-type compound, IrSi. Analysis of the bonding scheme and DFT-Chemical Pressure (CP) distribution of the reported MnP-type structure exposes issues pointing towards new structural behavior. The placement of the Fermi energy below an electronic pseudogap indicates that this structure is electron poor, an observation that can be traced via the 18−*n* rule to the structure's Ir-Ir connectivity. In parallel with this, the structure's CP scheme highlights facile paths of atomic motion that could enable a structural response to this electronic deficiency. Combined, these analyses suggest that IrSi may adopt a more complex structure than previously recognized. Through synthesis and detailed structural investigation of this phase, we confirm this prediction: single-crystal X-ray diffraction reveals an incommensurately modulated structure with the (3+1)D superspace group $P2_1/n(0\beta\gamma)00$ and $\mathbf{q} \approx -0.22\mathbf{b}^* + 0.29\mathbf{c}^*$. The structural modulations increase the average number of Ir-Ir bonds to nearly match the 18−*n* expectations of the phase through Ir-Ir trimerization along negative CPs, with the incommensurability arising from the difficulty of contracting and stretching the Ir-Ir contacts in a regular pattern without expanding the structure along directions of negative Si-Si CP. Integrating these results with prior analyses of related systems points to a simple guideline for materials design, the Frustrated and Allowed Structural Transitions (FAST) principle: the ease with which competing structural phenomena can be experimentally realized is governed by the degree to which they are supported by the coordination of the atomic packing and electronic factors.

1. INTRODUCTION

As quantum mechanical objects, molecules must navigate complex potential energy surfaces—dictated by the competing desires to maximize favorable orbital overlaps and to minimize repulsive forces at nonbonded contacts—to achieve the most stable geometries and the lowest energy reaction paths. And yet, such is the chemical imagination that chemists can often discuss these phenomena fluently referencing just two terms: sterics and electronics. The situation is more complicated for inorganic extended structures. For example, in intermetallic compounds, it has long been known that these same factors underlie a diverse structural chemistry.[1-3] This is vividly demonstrated by structure maps that show clustering of structure types in spaces defined by a variety of atomic properties, including valence electron count and atomic size, suggesting that different configurations have stability ranges with respect to these parameters.[4-8] However, while such maps and the data they contain provide excellent input for seeing trends and data-mining approaches, they themselves provide no chemical interpretations that could be applied to new structural chemistry.

Indeed, the formation of many complex structures beyond existing structure maps seems to originate from the interplay of electronics and atomic packing, but the exact roles these factors play often remain unclear. For instance, although $BaAl_4$-type compounds typically prefer 14-electron counts, the stabilization of the structure type with fewer electrons in $SrAu_xIn_{4-x}$ and $SrAu_xSn_{4-x}$ is attributed to the incorporation of smaller Au atoms.[9] Similarly, the homogeneity ranges of $A_9Zn_{4+x}Pn_9$ and $A_9Cd_{4+x}Pn_9$ (A = Ca, Sr, Yb, Eu; Pn = Sb, Bi) are thought to emerge from the conflict between atomic size constraints and the need for Zn/Cd stuffing atoms for charge balancing,[10] while similar tensions are thought to underlie superstructure formation in Sr_3In_{11}.[11] However, the reliance of these analyses on empirical observations makes it difficult to predict such structural phenomena in new systems.

Recent theoretical developments have established more direct links between local structural features in intermetallics and electronics and size effects. Bonding schemes such as the Zintl-Klemm concept[12,13] and the 18−*n* rule[14,15] provide prescriptions for the numbers of different interatomic contacts needed to achieve closed shells for a given composition. In parallel with this, the DFT-CP method[16-19] enables one to visualize frustrations that can arise within dense atomic packings, from which the role of atomic size can be assessed. Analyzing these two aspects of a system together can take us a long way in understanding complex structural phenomena. For example, the Nowotny Chimney Ladders adopt a wide range of stoichiometries governed by an ideal electron count[20-22] traceable to the

18−*n* rule.[14] Meanwhile, the CPs outline a helical path of soft atomic motions, which allow the stoichiometries to be nearly continuously varied[23] and lead to bihelical structures. A closely related example is the weakly ordered compound, Fe_2Al_5, where non-stoichiometry is required to reach the ideal 18−*n* electron count of the phase. This non-stoichiometry is accommodated within channels of nearly continuous Al positions templated by the CP scheme, allowing for a tunable composition bounded roughly by the 18−*n* electron count.[24]

These two factors can also act in a more antagonistic manner. In the electronically-driven phase transition between the high-temperature fluorite-type form of $PtGa_2$[25] and its low-temperature tetragonal polymorph,[26] atomic packing tensions revealed by the CP scheme require the phase transition to happen in a tightly concerted manner. A highly hysteretic phase transition results, which can be stifled by interstitial Pt atoms for Pt-rich compositions.[27]

While these examples comprise diverse structural phenomena, there are commonalities among them: in each, the electronics motivate a variation on a relatively simple structure, while the CPs guide the specific geometrical route by which the electronics are satisfied. It seems, then, that such electronically-driven, CP-guided complexity might be anticipated to occur in other intermetallics where non-ideal electron counts occur alongside CP features suggestive of soft atomic motions. Using these guidelines, we considered where else this type of phenomenon might occur and identified the MnP structure type as a potential source of complexity: half of the twenty reported intermetallics are purported to crystallize as electron-poor compounds,[15] and the CP scheme outlines possible routes for atoms to move in response.

In this Article, we will illustrate how these indicators of tensions can indeed be used predictively, by anticipating and elucidating unrecognized structural chemistry in one such (nominally) MnP-type intermetallic compound, IrSi. Here, the need for new Ir-Ir interactions to satisfy the 18−*n* rule runs counter to negative pressures in the Si sublattice, setting the stage for incommensurate modulations. As we will conclude, our ability to forecast complexity in the case of IrSi, combined with our earlier analyses of other systems, points to a simple strategy for materials design in intermetallics, which we call the Frustrated and Allowed Structural Transitions (FAST) principle—superstructures, structural progressions, and phase transitions are most favorable when the electronic and atomic packing factors work together, while the opportunities for such behavior to emerge becomes limited when the different driving forces conflict.

2. EXPERIMENTAL

2.1. Bonding Analysis of MnP-type IrSi. The bonding scheme of MnP-type IrSi was analyzed with the reversed approximation Molecular Orbital (raMO) method.[28] First, the geometry was optimized with the framework of DFT, using the Vienna Ab initio Simulation Package (VASP)[29-32] and Perdew-Burke-Ernzerhof (PBE)-GGA functionals.[33-36] The calculations were performed in the high-precision mode using the projector augmented wave (PAW) potentials provided with the package,[37,38] with a 5×10×5 Γ-centered k-point grid and an energy cutoff of 245.3 eV. Next, single-point calculations were performed on the optimized geometry to obtain band energies and projected density of states (DOS) distributions to serve as the basis for the calibration of a simple Hückel model for the compound with the eHtuner program;[39] the final parameters can be found in the Supporting Information. The resulting parameters were then used in simple Hückel calculations with YAeHMOP[40] on a 2×4×3 supercell of MnP-type IrSi, such that multiple *k* points in the Brillouin zone are mapped to the Γ point. The Γ-point Hamiltonian matrix for the supercell was then imported into the in-house Matlab program makeramo for the raMO analysis.

2.2. DFT-Chemical Pressure Analysis. The DFT-Chemical Pressure scheme was calculated for MnP-type IrSi to investigate atomic packing tensions within the structure. The structure was first optimized with LDA-DFT using the ABINIT[41-44] software package and Hartwigsen-Geodecker-Hutter norm-conserving pseudopotentials.[45] Single-point calculations were then performed on the optimized geometries at the equilibrium volume, as well as at slightly contracted (−0.05%) and expanded (+0.05%) volumes. These calculations yielded the kinetic energy and electron densities, as well as the local components of the Kohn-Sham potential used to produce the 3D chemical pressure maps.

Next, the ABINIT output was used to calculate CP maps with *CPpackage2*, using core unwarping with tricubic interpolation[16] and the mapping of the non-local pseudopotential energies.[19] The CP maps were partitioned into contact volumes between atom pairs using the Hirschfeld-inspired integration scheme,[16] and the pressures within each contact volume was averaged and projected onto atom-centered spherical harmonics ($l \leq 4$). The final CP schemes were visualized with Figuretool2, an in-house Matlab application. During the core unwarping and contact volume construction steps, Bader charges, extracted from the PAW-GGA electronic structures using the Bader program,[46-49] were used to account for electron transfer between Ir and Si. Then free ion electron densities were generated with the Atomic Pseudopotential Engine (APE)[50] for a range of percentages of the Bader charge (0 to 50%, beyond which convergence issues emerged). The CP schemes in the main text used the free ion electron densities for 50% of the Bader charges; the other results are given in the Supporting Information.

2.3. Spin-Orbit Coupling. For the main text, theoretical results were calculated without the inclusion of spin-orbit coupling (SOC). However, due to Ir's large nuclear charge, we carried out additional calculations factoring in SOC to investigate any impact it might have on our conclusions. In the Supporting Information we present comparisons of the DOS distribution for MnP-type IrSi calculated using ABINIT with and without spin-orbit coupling. The features near the Fermi energy (E_F) are largely unaffected by SOC. A CP scheme for MnP-type IrSi with spin-orbit coupling included is also provided in the Supporting Information, showing that the overall features of the scheme are maintained. Spin-orbit coupling, thus, does not significantly affect our conclusions.

2.4. Synthesis. IrSi was prepared by reaction of the component elements at stoichiometric and slightly off-stoichiometric (Ir:Si ratios of 1:0.8 and 1:1.2) ratios. Ir and Si powders (Ir: Alfa Aesar, 99.9%; Si: Alfa Aesar, 99.99%) were weighed out, pressed into pellets in an Ar-filled glovebox, and arc-melted three times on alternating sides for 10 s each to maximize homogeneity. The ingots were then placed in fused silica tubes, which were sealed under vacuum and annealed at 600 °C, 800 °C, or 1000 °C in a muffle furnace for 1 week. After the annealing period, the samples were quenched in ice water or cooled to room temperature at a rate of 20 °C/hr.

2.5. Powder X-ray Diffraction. Samples were prepared for phase analysis with powder X-ray diffraction by grinding fragments of the samples using an agate mortar and pestle. The fine powders were mounted on a zero-background Si plate and analyzed with a Bruker D8 Advance Powder Diffractometer using Cu Kα radiation (λ = 1.5418 Å) over a 2θ range of 15−90° in increments of 0.02° at an exposure time of 0.9s. Powder X-ray diffraction patterns were also collected using synchrotron radiation at beamline 11-BM at the Advanced Photon Source to better detect and resolve potential satellite peaks. Patterns were collected at three temperatures: 100 K, 295 K, and 460 K. No additional polymorphs were evident at these temperatures. The powder patterns for the sample that yielded the single crystal discussed in the main text is provided in the Supporting Information.

2.6. Elemental Analysis via Energy Dispersive X-ray Spectroscopy (EDS). Samples were prepared for EDS by embedding pieces of the fragmented ingots in epoxy. After curing the epoxy for 24 hrs at 65 °C, the specimens were polished with diamond lapping film at increasingly fine grit, from 9 μm to 0.5 μm. Finally, the samples were coated with a 20 nm layer of carbon to increase conductivity. The samples were imaged and analyzed in a Hitachi S3400-N scanning electron microscope (voltage of 30 keV) equipped with an EDS detector.

2.7. Differential Scanning Calorimetry (DSC). DSC experiments were performed with a Netzsch Pegasus 404 differential scanning calorimeter. Experiments were run with a 10 °C/min heating rate under a nitrogen gas flow of 50 mL/min, cycling two times between 100 °C and 1000 °C. The data were analyzed using the Netszch Proteus software provided with the instrument. The results show no evidence of transitions for IrSi over this temperature range.

2.8. Single-Crystal X-ray Diffraction. Single crystals were picked and then analyzed with an Oxford Diffraction Xcalibur E diffractometer equipped with a Mo Kα (λ = 0.71073 Å) sealed-tube X-ray source at room temperature. To sufficiently separate the main reflections and satellite peaks, the detector-to-crystal distance was set to 100 mm. The data was collected at an exposure of 120 s/0.5°. Run list generation and frame data processing were performed using the CrysalisPro software[51] supplied by the manufacturer. The charge flipping algorithm,[52,53] as implemented in the program SUPERFLIP,[54] was used to obtain the initial structural solution. The solution was modeled and refined on F^2 in JANA2006.[55] The refined structural parameters are listed in the Supporting Information, while the Crystallographic Information File (CIF) can be obtained from the Cambridge Crystallographic Data Centre (deposition number: CSD 1956234).

3. RESULTS AND DISCUSSION

3.1. Preliminary theoretical analysis of MnP-Type IrSi. During our screening of simple transition metal (T)- main group metal (E) structures for those that frequently violate electron counting rules while exhibiting atomic packing issues, the MnP type emerged as a potential source of structural chemistry. In this structure, the T-T connectivity is expected to follow the 18–*n* rule, where each T atom aims to reach an 18-electron configuration by sharing electrons through *n* number of bonding functions isolobal to traditional 2-center 2-electron functions. The T atoms build up a flattened diamond network, allowing each T atom to form four T-T close contacts in a distorted tetrahedral environment (purple lines in Figure 1). As such, compounds in the MnP type follow the 18–*n* rule when they have 14 electrons/T atom (n = 4).[15] However, ten of the twenty reported MnP-type compounds, including the prototype phase MnP itelf,[56] fall short of this 18–*n* ideal electron count, with valence electron counts of 13 electrons/T atom or lower.

For example, IrSi (whose component elements we happened to have on hand), has a valence electron count of 13 electrons/Ir atom (9+4 = 13 electrons/Ir), deficient by one electron relative to the 14-electron ideal. A calculation of IrSi's electronic density of states (DOS) distribution (Figure 1b) confirms this expectation. The Fermi energy (E_F) falls a little below the deep DOS minimum associated with the 18–*n* count, highlighting the phase's electron-poor character. Further investigation of the bonding in IrSi with the reversed approximation Molecular Orbital (raMO) method, shown in the Supporting Information, reveals π-contributions to the Ir-Ir bonding, a sign of unsaturated interactions.

This electron deficiency hints at possibilities for structural chemistry. For instance, incorporating more Si atoms would bring additional electrons to the structure, while forming more Ir-Ir bonds would lower the number of electrons required to reach an 18-*n* count. Both options would go some way toward making IrSi electron precise. How feasible are they?

To see whether atomic packing effects might support any of these options, we turned to the DFT-Chemical Pressure (CP) analysis,[16-19] which resolves the macroscopic internal pressures of an intermetallic into two-atom pressures that desire either expansion (positive pressures) or contraction (negative pressures) of the structure. IrSi's CP scheme is overlaid on a section of the structure in Figures 1a,c. Negative Ir-Ir CPs (black lobes) run parallel to the long contacts along *b* (shown as dotted purple lines in Figure 1c) and negative Si-Si CPs follow the Si zigzag chain. Positive Ir-Si CPs (white lobes) on the Si are oriented nearly perpendicular to the negative CP features along *b*, giving the distribution quadrupolar character.

CP quadrupoles like these have a qualitative connection to the vibrational properties of atoms within a solid.[57,58] Motions along the negative pressures of a CP quadrupole are expected to be soft, as they shorten overly long contacts while potentially lengthening contacts of positive CP. Such motions could allow the formation of new Ir-Ir interactions along *b*, making this a viable route to handling the electron deficiency (though concerted motion of the Si atoms would be required to avoid shortening the Ir-Si contacts). Incorporation of additional Si atoms also remains a possibility: the negative CPs along the zigzag chain could incorporate new atoms, but large motions within the structure would be needed to make space for these atoms.

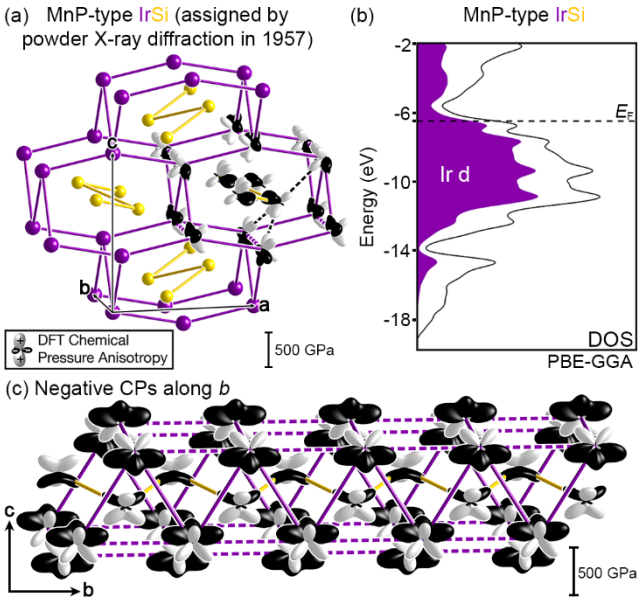

Figure 1. The reported crystal structure of IrSi. (a) The MnP-type IrSi structure previously solved by powder methods overlaid with its DFT-Chemical Pressure (CP) scheme. (b) The density of states (DOS) curve for MnP-type IrSi, with the Fermi energy (E_F) falling below a deep pseudogap. (c) A hexagonal channel of the MnP-type structure viewed along the *b*-axis, highlighting negative CPs parallel to the long Ir-Ir contacts in this direction (dashed purple lines).

These electronic and atomic size considerations suggest that there may be more complexity to IrSi's structure than has been previously recognized. In fact, the structure of IrSi has never been refined from single crystal studies. It was first assigned to the orthorhombic MnP type in 1957,[59] and two later studies (in 1970[60] and 1993[61]) focused on charting the Ir-Si phase diagram—all based on powder X-ray diffraction. In 1995,[62] Görannsson, et al. refined the structure from powder data using the Rietveld method, achieving an R-value of 13%. Weaker reflections associated with superstructures,

such as the variations we are envisioning for IrSi, are often difficult to detect using powder techniques, particularly on standard laboratory diffractometers. To explore its potential to exhibit new structural chemistry, we thus set out to find single crystals of IrSi.

3.2. Synthesis and characterization. To synthesize IrSi, we arc-melted and annealed pellets of the mixed metals at compositions near the target 1:1 stoichiometry. All syntheses resulted in brittle silvery-gray ingots whose major powder X-ray diffraction peaks could be indexed to MnP-type IrSi. Peaks corresponding to nearby binaries were also detected, except for one sample loaded at a 1:0.8 stoichiometry and annealed at 600 °C (see the Supporting Information). However, weak reflections invariably appeared at $2\theta \approx 42°$ and 47° that did not match any known phases, hinting that the strongest peaks of the powder pattern do not tell the full story.

Compositional analysis of the sample with energy-dispersive X-ray spectroscopy (EDS) confirms the presence of an approximately 1:1 phase and the nearby binaries Ir_3Si_2, Ir_4Si_5, or Ir_3Si_4, depending on loading composition (see the Supporting Information). The EDS compositions of $IrSi_{1.06(3)}$, $IrSi_{1.06(1)}$, and $IrSi_{1.066(9)}$ for three different samples (Si-poor, stoichiometric, and Si-rich, respectively) suggests that the structure is not inserting substantial numbers of additional Si atoms; reaching the ideal electron count in this manner would require an Ir:Si ratio of 1:1.25. These analyses confirm our successful synthesis of a 1:1 IrSi phase, whose major features align with previous reports. Let's now turn to single-crystal X-ray diffraction for a more detailed investigation of the structure.

3.3. Diffraction patterns of IrSi. Unit cell runs of nearly 50 crystals selected from our samples consistently returned the MnP-type orthorhombic unit cell. However, when a hemisphere of data was collected at longer exposure times, signs of greater complexity became apparent. The orthorhombic lattice only accounts for approximately half of the observed peaks. The reciprocal lattice layer reconstructions of this data, such as the *0kl* layer shown in Figure 2, reveal that the remaining reflections are less intense satellites emanating from the main reflections. As can be seen in the insets of Figure 2a, many of the main peaks are surrounded by a rectangle of four more distant satellites, as well as a pair of closer satellites. Such features indicate that IrSi is, in fact, subject to incommensurate modulations.

At first, the diffraction pattern suggests that four vectors (labeled $\mathbf{q}_1$, $\mathbf{q}_1'$, $\mathbf{q}_2$, and $\mathbf{q}_2'$) beyond the usual reciprocal lattice grid are required for full indexation of these features. However, given the orthorhombic symmetry of the basic lattice, it is likely that domains with an off-axis modulation, such as $\mathbf{q}_1$, would coexist with other twin domains with **q**-vectors related by symmetry elements of the basic lattice, i.e. $\mathbf{q}_1'$. Indeed, while screening single crystals, one very small specimen (longest side <0.02 mm) showed a diffraction pattern with only satellite reflections associated with $\mathbf{q}_1$ and $\mathbf{q}_2$, confirming the notion that $\mathbf{q}_1'$ and $\mathbf{q}_2'$ arise from a twin domain that reflects the diffraction pattern across the **a***__b__*-plane. With that discovery, we can now index the most intense set of satellite reflections with the vector $\mathbf{q}_1 \approx -0.22\mathbf{b}^* + 0.29\mathbf{c}^*$, shown as a red arrow in Figure 2a. A small number of satellite reflections from this domain can also be indexed to $\mathbf{q}_2 \approx -0.10\mathbf{b}^* + 0.07\mathbf{c}^*$, indicated by the yellow vector. From there, $\mathbf{q}_1'$ and $\mathbf{q}_2'$ are attributed to twinning.

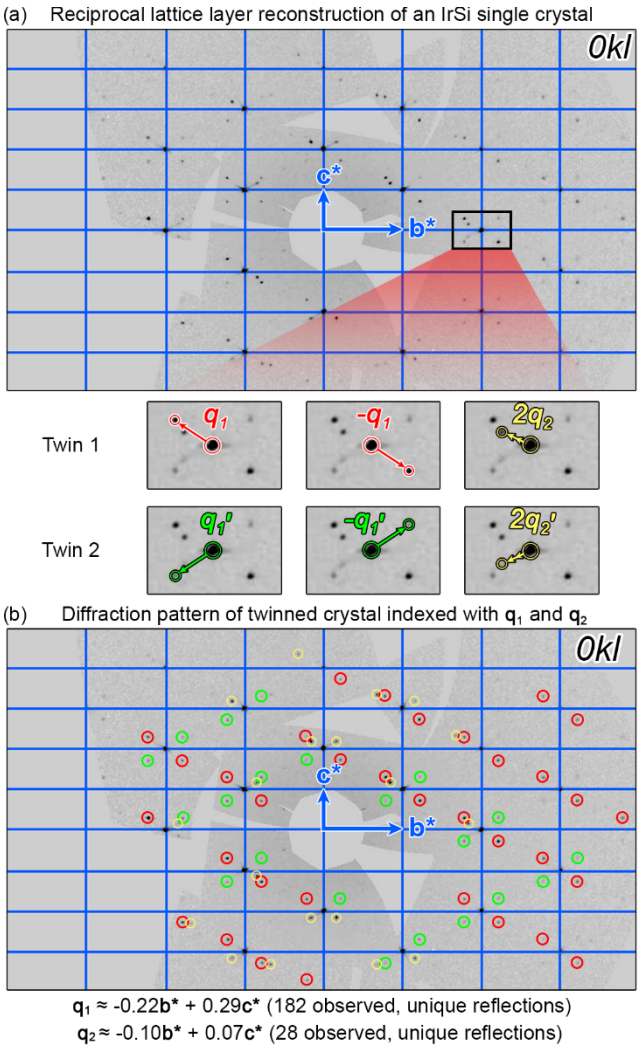

Figure 2. Reconstruction of the *0kl* reciprocal lattice layer from X-ray diffraction data collected on an IrSi single crystal. (a) The main reflections define a primitive orthorhombic cell (blue grid) consistent with an underlying MnP-type basic cell. Satellite reflections are indexed as $\mathbf{q}_1$ and $\mathbf{q}_2$, or their twinned versions, $\mathbf{q}_1'$ and $\mathbf{q}_2'$. (b) The indexed diffraction pattern, with $\mathbf{q}_1$ reflections circled in red, $\mathbf{q}_1'$ reflections circled in green, and $\mathbf{q}_2$ and $\mathbf{q}_2'$ peaks circled in yellow.

As shown in Figure 2b, the entire pattern can now be indexed. The peaks ascribed to $\mathbf{q}_1$ are circled in red, while the twin reflections associated with $\mathbf{q}_1'$ are circled in green. Yellow circles surround peaks indexed with $\mathbf{q}_2$ and $\mathbf{q}_2'$. Inspection of the peaks circled in red and green shows that $\mathbf{q}_1$ reflections are generally more intense than the $\mathbf{q}_1'$ reflections, a trend that holds for the $\mathbf{q}_2$ reflections as well. It appears, then, that the domains giving rise to the $\mathbf{q}_1'$ and $\mathbf{q}_2'$ satellites represent a minor component in the crystal. Furthermore, note that relatively few peaks are assigned to $\mathbf{q}_2$ and $\mathbf{q}_2'$ (yellow), a feature that was seen for all 10 crystals for which we collected full datasets. In fact, this dataset contains 182 observed, unique $\mathbf{q}_1$ reflections compared to only 28 for $\mathbf{q}_2$. Taken together, these features of the diffraction pattern suggest that the primary modulation affecting the crystal is encoded in the $\mathbf{q}_1$ peaks.

The fully indexed diffraction pattern irrevocably shows that, at least at room temperature, IrSi is not crystallizing in the simple MnP type, but instead adopts an aperiodic structure with two additional periodicities acting on the basic orthorhombic lattice.

3.4. IrSi's basic structure. To uncover any clues they may provide about the nature of the modulations, let's focus first on the main reflections. These arise from the primitive orthorhombic basic cell with lattice vectors $a \approx 5.56$ Å, $b \approx 3.22$ Å, and $c \approx 6.28$ Å (matching the previous reports of IrSi's unit cell). Integration of these reflections and solution in the space group *Pnma* proceeds smoothly, resulting in the expected MnP-type average structure. In fact, the refinement of the average structure yields a very good model with $R(I>3\sigma) = 2.75$ and GOF = 1.69, as well as acceptable residual Fourier electron densities, with $\Delta\rho_{max}$ and $\Delta\rho_{min}$ = 2.91 and -2.46 electrons/Å^3, respectively. The quality of the refinement highlights how easily the incommensurability could be overlooked here if the satellites were not detected. The only noteworthy feature of the refinement is an elongation of the Ir thermal ellipsoids along *b*. While this elongation is not severe enough that it would cause alarm during a typical structural determination, it suggests atomic motions along this direction could play a role in the modulated structure.

3.5. The (3+1)D solution of modulated IrSi. We are now ready to include the crystallographic information encoded in the satellite peaks. To do this, we turn to superspace crystallography, in which the aperiodic three-dimensional crystal is embedded in a (3+*d*)-dimensional space, where "*d*" refers to the additional dimensions, perpendicular to physical space, required to construct a higher-dimensional periodic lattice and apply its symmetry to the crystal.[63] The diffraction patterns of IrSi suggest that a solution in (3+2)D superspace is required to capture the full story. However, the data for the $\mathbf{q}_2$ modulation are very sparse, giving little basis for the modeling and refinement of the $\mathbf{q}_2$ modulation. The limited data for $\mathbf{q}_2$ peaks was a common theme across a wide number of crystals, and all attempts to model the $\mathbf{q}_2$ modulations resulted in high R-values for the $\mathbf{q}_2$ satellites. With these difficulties in mind, as well as the ambiguity as to whether $\mathbf{q}_2$ coexists with $\mathbf{q}_1$ in the same domains or represents another domain type in the crystal, the structural model presented below is solved in (3+1)D and only includes data from $\mathbf{q}_1$.

Our next step is to assign the (3+1)D superspace group of the structure. The highest possible space group can be derived by first considering which symmetry operations of the MnP type's *Pnma* space group are compatible with the **q**-vector. $\mathbf{q}_1 \approx -0.22\mathbf{b}^* + 0.29\mathbf{c}^*$ breaks the symmetry associated with the $\mathbf{b}^*$ and $\mathbf{c}^*$ directions, reducing the symmetry of the modulated structure to a monoclinic subgroup of *Pnma* with *a* being the unique axis. Thus, any symmetry operations at work in the modulated structure should be derived from the 3D space group $P2_1/n11$.

Embedding the symmetry elements of $P2_1/n$ into (3+1)D space introduces the possibility of translational components along the newly introduced dimension, x_4. In particular, the *n* glide perpendicular to *a*, $(x, y, z) \longrightarrow (-x, y + \frac{1}{2}, z + \frac{1}{2})$, can be embedded in superspace as either $(x_1, x_2, x_3, x_4) \longrightarrow (-x_1, x_2 + \frac{1}{2}, x_3 + \frac{1}{2}, x_4)$ or $(x_1, x_2, x_3, x_4) \longrightarrow (-x_1, x_2 + \frac{1}{2}, x_3 + \frac{1}{2}, x_4 + \frac{1}{2})$. These can be distinguished using systematic absences, with the latter requiring the reflection condition $0klm$: $k+l+m=2n$. No such condition is evident in the diffraction data. In fact, no other reflection conditions beyond those expected for $P2_1/n$ were present. The resulting (3+1)D space group is therefore $P2_1/n11(0\beta\gamma)00$, where "$(0\beta\gamma)$" indicates that the **q**-vector has irrational components along $\mathbf{b}^*$ and $\mathbf{c}^*$, and "00" signifies that there are no glides along x_4 associated with the generating operations (the 2_1-screw axis parallel to *a* and the *n* glide perpendicular to *a*). As we will see below, this space group is confirmed by the structural solution and refinement of IrSi's structure (Table 1).

Table 1. Crystallographic Information for IrSi

Refined Composition	IrSi
Composition from EDS	$IrSi_{1.06(3)}$
Crystal Dimensions (mm)	0.061×0.030× 0.025
Crystal Color	silver
Radiation Source, λ (Å)	0.71073
Absorption Correction	analytical
Data Collection Temp.	RT
(3+1)D Superspace Group	$P2_1/n(0\beta\gamma)00$
a (Å)	5.5573(16)
b (Å)	3.2210(11)
c (Å)	6.278(2)
$\alpha = \beta = \gamma^a$	90°
q vector[b]	(0, -0.2157(6), 0.2888(10))
Cell Volume (Å^3)	112.38(6)
Absorption Coefficient (mm^{-1})	118.922
θ_{min}, θ_{max}	4.884, 27.015
Refinement Method	F^2
R_{int}(I>3σ, all)	3.36, 4.29
Statistics for Main Reflections	
Unique Reflections ($I > 3\sigma$, all)	160, 235
$R(I>3\sigma)$, $R_w(I>3\sigma)$	2.89, 6.20
R(all), R_w(all)	3.71, 6.38
Statistics for Satellite Reflections, m=1	
Unique Reflections ($I > 3\sigma$, all)	181, 302
$R(I>3\sigma)$, $R_w(I>3\sigma)$	4.25, 8.41
R(all), R_w(all)	11.34, 14.03
Statistics for Overall Refinement	
Number of Reflections	1880
Number of Parameters	37
Unique Reflections ($I > 3\sigma$, all)	341, 718
$R(I>3\sigma)$, $R_w(I>3\sigma)$	3.31, 6.63
R(all), R_w(all)	6.33, 8.38
$S(I>3\sigma)$, S(all)	1.23, 1.04
$\Delta\rho_{max}$, $\Delta\rho_{min}$ (e$^-$/Å^3)	3.59, -3.81

[a]To allow refinement of the average and modulated structures using the same reflection set, the unit cell angles were restrained to 90° to match the orthorhombic symmetry of the average structure.

[b]For the structure refinement, the **q**-vector was rounded to (0, -0.22, 0.29) to better reflect the precision with which this vector is known.

With the superspace group assigned, an initial model of the (3+1)D structure was obtained with the charge-flipping algorithm. The charge-flipping iterations quickly converged on a (3+1)D electron density that matched the symmetry of the assigned space group. The initial result correctly assigned the atomic position for Ir while the initial atomic position for Si was assigned with the peak-search

function of JANA2006.[55] In this first solution, there is a single symmetry distinct position for each element, Ir1 and Si1, with a refined composition of IrSi.

After we modeled the positional modulation of both atomic positions with harmonic functions, refinement of the structure led to an overall $R(I>3\sigma)$ of 3.36 (Table 1). While this value is somewhat larger than that for the average structure, $R(I>3\sigma) = 2.75$, this stems from the incorporation of the relatively weaker satellite reflections in the refinement, as can be seen from the $R(I>3\sigma)$ values for the main reflections and first order satellites, 2.89 and 4.25, respectively. Furthermore, a simulated powder X-ray diffraction of the modulated structure now accounts for the previously unassigned peaks at $2\theta \approx 42°$ and 47° as $(hklm) = (103\bar{1})$ and $(211\bar{1})$, respectively. Powder patterns collected with synchrotron radiation at 100 K, 295 K, and 460 K also match this assignment (see the Supporting Information).

Comparison of the atomic positions in the model to the corresponding features in the (3+1)D Fourier maps provides further confirmation of its validity. In the Fourier map (Figure 3), the atomic positions are evident as continuous strings of electron density running along x_4, which represents the phase of the modulation function. The x_4 axis is oriented perpendicular to physical space. As such, the non-modulated axis, x_1, lies parallel to the physical x axis (in this context, x, y, and z refer to the fractional coordinates of atoms along the a, b, and c directions of the basic cell in physical space); traveling along x_1 corresponds to motion along the physical x axis. On the other hand, x_2 and x_3 are tilted out of physical space; a translation along x_2 or x_3 then requires a shift along x_4 to stay in physical space.

We begin with the Ir1 site's model in Figure 3a, with the black lines showing contours of the observed Fourier electron density and the thicker purple line representing our refined model, comprised of two harmonic modulation waves. Along the x_1 direction, the atomic position stays nearly unchanged compared to the average structure. However, the Ir positions along the x_2 and x_3 directions show significant deviations away from the average position, with maximum widths of 0.40 Å and 0.23 Å, respectively.

Similar plots are shown in Figure 3b for the Si1 site, where now a single harmonic wave is sufficient to trace the shape of the electron density (shown in gold). As before, the Si positions along the x_1 direction appear non-modulated, while along the other two directions they oscillate around the average structure, with maximum widths of 0.19 Å and 0.30 Å for x_2 and x_3, respectively.

3.6. Ir modulations viewed in 3D. With our (3+1)D crystallographic model of IrSi's structure in hand, we can now analyze how the modulations address the steric and electronic tensions afflicting the average structure. Let's start with the largest perturbation away from the MnP-type average structure: the Ir positional modulation along x_2 (Figure 4). In Figure 4a, we show how the physical y-axis (red arrow) crosses through the x_2-x_4 plane, sampling the Ir modulation waves (purple lines) at different points. Each point where this cut intersects with an Ir atom's modulation function represents the location of an Ir atom in physical space. Since x_2 is tilted off of y, changing x_2 requires displacement along x_4 in order to remain in physical space. Thus, each new Ir atom along y appears at a different x_4 value and is displaced relative to the average position (dotted line) by different amounts. The structural consequence is a chain of unevenly spaced Ir atoms, with distances either contracted or lengthened relative to the average (3.22 Å). For example, in the middle of the plot are two contacts shortened significantly compared to the average structure with distances of 3.04 Å and 3.09 Å along y.

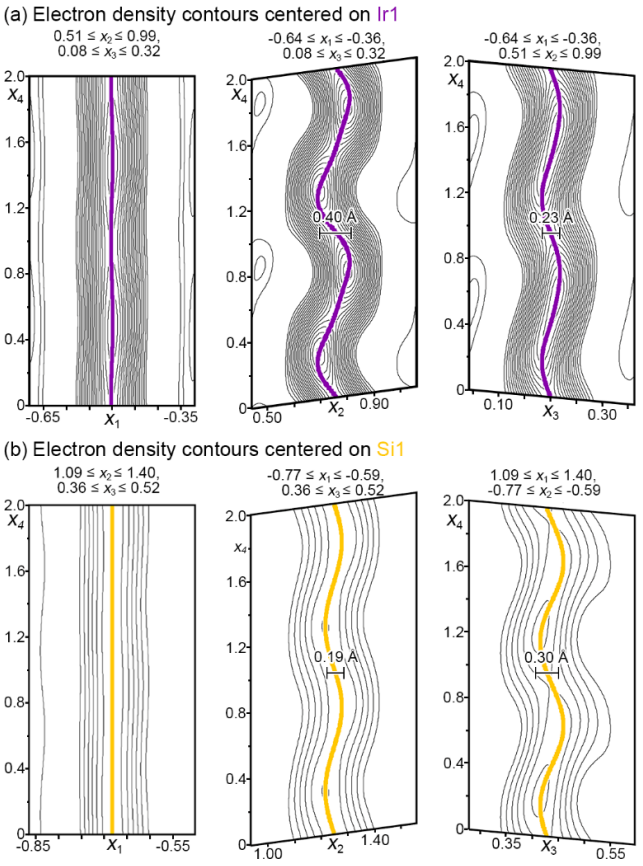

Figure 3. Modeling the electron density of IrSi in (3+1)D superspace. (a) Electron density plots of the Ir1 site's motion along x_1, x_2, and x_3 as a function of x_4. In each plot, the electron density is summed over a 1.5 Å thick width over the other directions. The purple line represents the model's Ir positions. (b) Plots of the Si1 position as a function of x_4, summing over 1 Å along the other two directions. The gold line represents the model's Si positions. Contour intervals: 3 electrons/Å^3.

By putting this chain of Ir atoms into its broader context within the structure (Figure 4b), we begin to see how the coordination environments of the Ir atoms are affected by the modulation along b. Contacts that have contracted more than 0.1 Å (shorter than 3.12 Å) are drawn with full purple lines, while longer contacts are shown with dashed lines. As in the average structure, each Ir atom retains the original four Ir-Ir interactions that form a distorted tetrahedral environment. Now, though, new short Ir-Ir contacts have appeared along b, resulting in an Ir trimer at the center. The formation of these additional short Ir-Ir interactions by the modulation is in accord with our earlier bonding analysis, where each Ir atom needed to participate in one additional Ir-Ir bond on average to reach its ideal 18–n

electron count. In fact, zooming out to a larger section of the structure (Figure 4c) shows that such Ir trimers are a dominant structural motif, forming tilted regions of Ir-Ir contraction and expansion within the *bc*-plane.

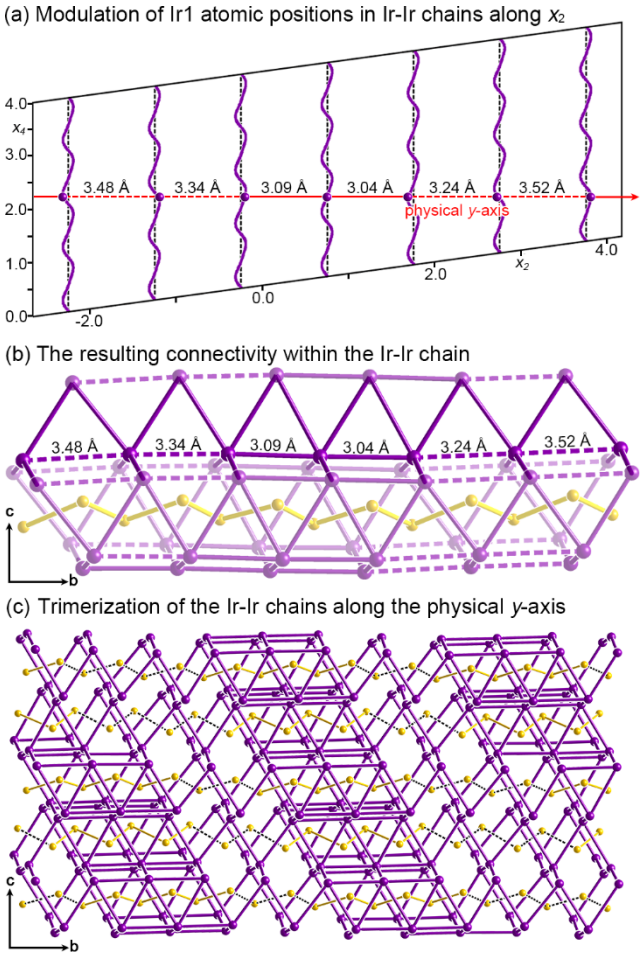

Figure 4. Effect of the modulation on the Ir connectivity. (a) The modulation functions for a chain of Ir atoms, plotted in the x_2-x_4 plane. An Ir atom is located at each point where the physical *y*-axis (red arrow) intersects the Ir modulation function, resulting in the Ir-Ir distances shown. Distances shorter than <3.12 Å are shown as full red lines, while longer contacts are shown as dashed lines. (b) The uneven Ir atom spacing that results along *b*, shown in the context of the structure. (c) Viewed at a larger scale, the Ir sublattice shows a tendency towards trimerization.

The structural fragments shown above provide a snapshot of the possible Ir configurations; the entire range of possible geometries is defined within one period of the modulation function. In Figure 5a, we zoom in on the modulation of a single Ir atom, shown as a purple line, with the positional modulation along x_2 plotted as a function of x_4. By sampling this function from $x_4 = 0$ to $x_4 = 1$ at regular intervals (purple spheres), we can see how the modulation maps onto the Ir coordination environment. The Ir-Ir distances from each sphere are represented with narrow bars of various tints of purple, beginning at white for distances ≥3.22 Å and darkening until the distances decrease to 3.12 Å. These distances are longer than the sum of Ir's metallic radii (2.71 Å), though they fall within the typical range for short Ir-Ir contacts in other solid-state compounds (2.7 to 3.2 Å) in the Inorganic Crystal Structure Database.[64,65]

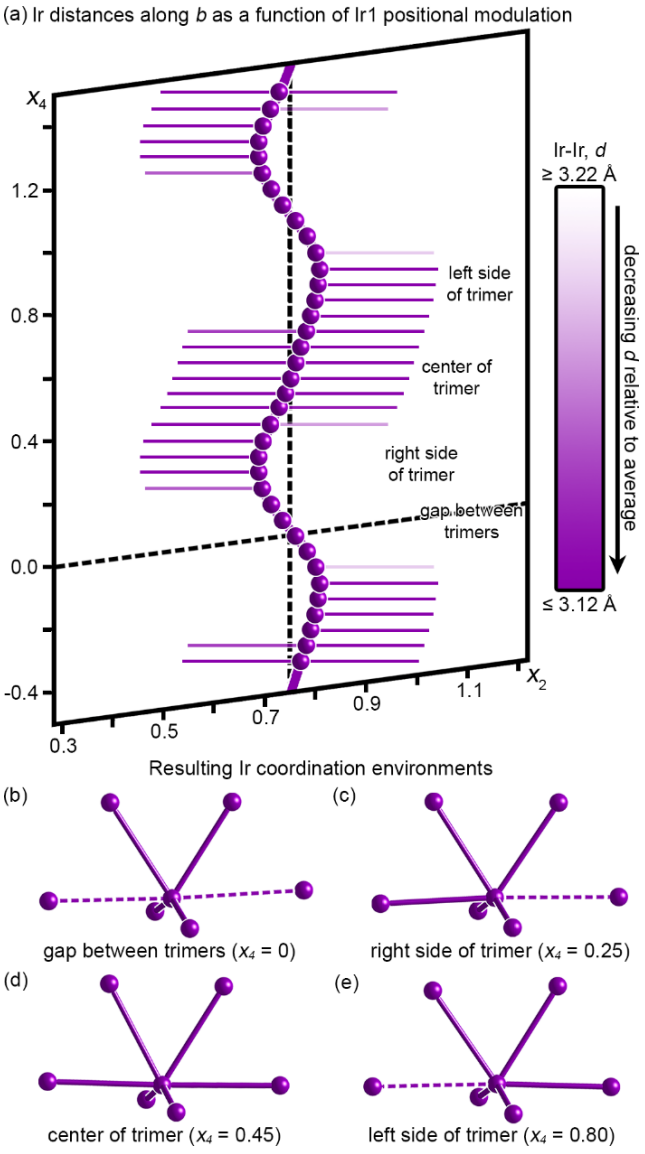

Figure 5. Modulation of the Ir-Ir connectivity in IrSi. (a) The positional modulation of an Ir atom along x_2 as a function of x_4. At intervals of 0.05 along x_4, Ir-Ir contacts to the left and right are represented by thin bars. The distances are shown as tints of purple. (b)-(e) The resulting coordination environments encoded in the modulation function, resulting in up to six Ir-Ir bonding interactions for a single Ir atom.

The Ir positions follow a nearly sinusoidal curve, consistent with the prominence of 1st order satellites in the diffraction pattern. However, a closer look reveals that the extrema of the curve are not evenly distributed: the regions of positive slopes are longer than those with negative slopes. At $x_4 = 0$ in Figure 5a, we begin at a shorter diagonal portion of the curve. In this region, we see gaps between trimers, i.e. the Ir atom has only a distorted tetrahedral Ir environment (Figure

5b). In the figure, these atoms have transparent bars on either side as both Ir-Ir distances have increased relative to the average. Traveling up x_4, we next reach a section of the function curved to the left of the average position; here, a purple bar connects the Ir atom to the Ir atom on its left (right side of a trimer, Figure 5c), so that $n = 5$ for these Ir atoms. Between $0.45 \leq x_4 \leq 0.75$, the modulation function flattens out to a long diagonal portion that is now slanted the other way. This region is the center of a trimer with contracted Ir-Ir distances on either side of the central atom ($n = 6$, Figure 5d), as is apparent in Figure 5 from the purple bars on both sides of the spheres. Finally, at $x_4 = 0.8$, the function curves to the right of the average position (Figure 5e), representing the left portion of the trimer with Ir atoms connected to their righthand Ir neighbor. Overall, the modulation function encodes four basic types of connectivity within the Ir chains along b: gaps between trimers, the right and left sides of a trimer, and the center of a trimer.

Such changes in the Ir-Ir connectivity should have consequences for the electronics of the phase.[66] Remember that for IrSi to follow the 18–n rule each Ir atom needs to gain on average one Ir-Ir interaction along b relative to the original MnP-type structure. We can use the relative lengths of the different portions of the modulation function to calculate a weighted average over these coordination types. At a quick glance, each of the coordination types appears to account for approximately ¼ of the period along x_4, suggesting a weighted average of 5 Ir-Ir bonds for each Ir atom. In fact, the average calculated from the sampling of x_4 presented in Figure 5 is 4.9, close to the ideal $n = 5$ we would expect from the 18-n electron count of this phase.

3.7. The CP-guided modulations of IrSi. It appears, then, that IrSi responds to the electronic needs of its parent structure by modulating its Ir positions along b, with a tendency for trimerization. While the trimerization matches the Ir-Ir connectivity with the structure's electron count, it does not represent the only way of having every Ir atom in a chain participate in one bond on average. For example, dimerization of the Ir atoms along b would achieve the same goal. Clues to the origins of the preference for trimers can be found in other structural aspects of the modulation, such as the displacements of the Si atoms and the direction of **q**. These details can be understood when viewed in terms of MnP-type IrSi's CP scheme.

As we saw in 3.1, the key tensions in the average structure's CP scheme (Figure 6a) are negative Ir-Ir CPs along b, negative Si-Si CPs along the Si zigzag chains, and positive Ir-Si CPs along the shortest heteroatomic contacts. The negative Ir-Ir CPs desire wholesale contraction of the structure along b. However, such an arrangement is undesirable for two major reasons: the structure only requires one additional Ir-Ir bond/Ir atom to reach its ideal electron count and contraction of an Ir-Ir distance also shortens neighboring Ir-Si contacts along directions of positive CP (red contacts in Figure 6a). Here, then, is one significant tension in the IrSi structure: balancing the desire for contraction of the Ir-Ir and Si-Si contacts with both the electronic needs of the system and the desire for expansion along heteroatomic contacts.

These issues are illustrated in Figure 6b: the Ir-Si contacts affected by positive CP trace out a buckled honeycomb network in the bc-plane (shown in red). The formation of new Ir-Ir contacts runs across the hexagons of this network, creating more tension between the Ir atoms and bridging Si atoms, urging them to move out of the way. In fact, in a model with the Si atoms fixed to their average position, the Ir modulations shrink the shortest Ir-Si distances by 0.2 Å to 2.20 Å. However, when allowed to modulate, the Si atoms move away from the Ir atoms along directions of negative CP during the formation of a short Ir-Ir interaction (an animation of these motions is available in the Supporting Information). The modulations lead to a range of Ir-Si distances, with some contacts shrinking to 2.34 Å—short, but still a remarkable improvement over the structure without Si modulations. It appears, then, that motions in the Si sublattice serve to maintain (or lengthen) Ir-Si distances as new Ir-Ir interactions are formed along b, similar to behavior seen in Y_3Ru_{2-x}.[67]

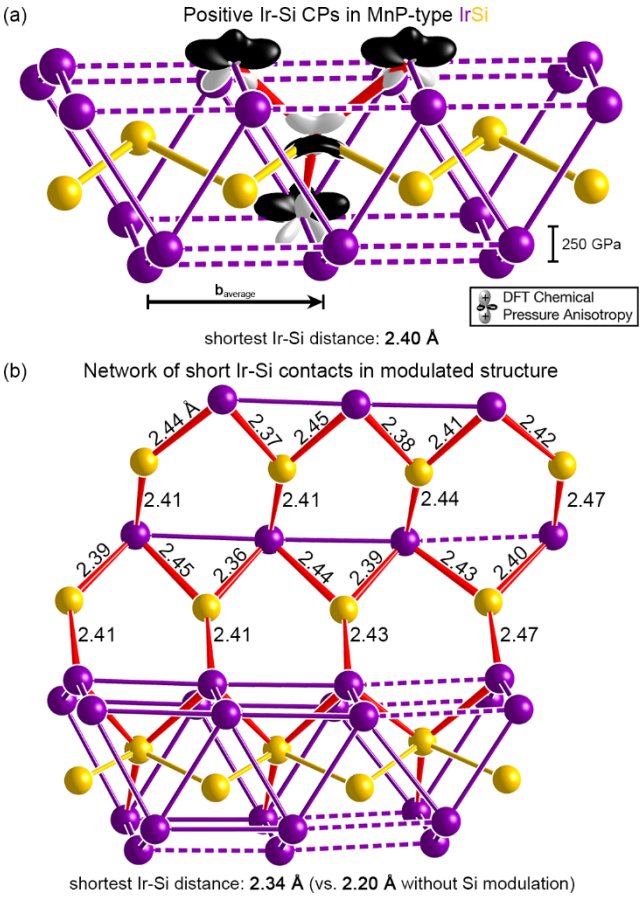

Figure 6. CP tensions between the Ir and Si sublattices. (a) A section of the average structure, with the Ir-Si contacts afflicted with positive CP highlighted with red lines. The shortest Ir-Si distance in the experimental average structure is 2.40 Å. (b) The Ir-Si positive CPs form a buckled honeycomb network in IrSi (red contacts within the context of a hexagonal channel). The shortest Ir-Si distance of this type is 2.34 Å but shrinks to 2.20 Å in a model with no Si modulations.

This coupling of Ir and Si motions along b sets up a CP issue with long-range consequences. In Figure 7a, we show this with a single Ir-Si chain of the average structure overlaid with its CP scheme. At this point, each Ir participates in no Ir-Ir bonds along b. We'll refer to

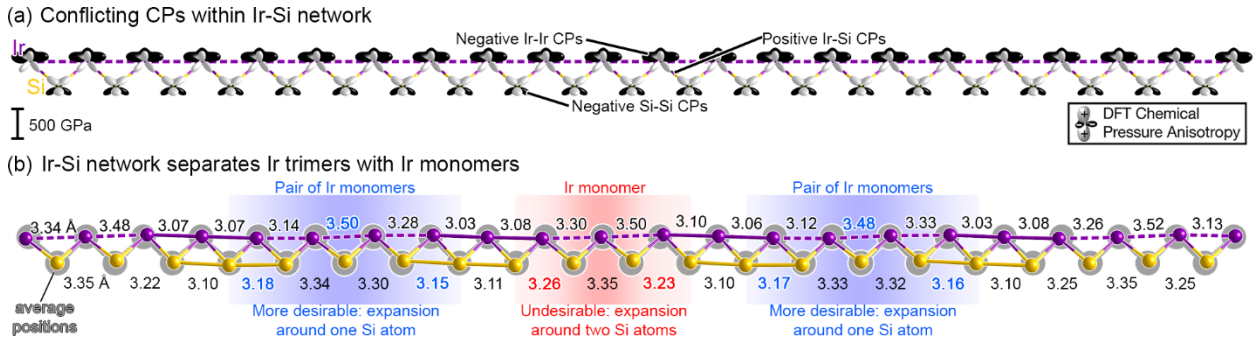

Figure 7. The CP-guided pattern of Ir-Ir trimerization along *b*. (a) Within the Ir-Si network, there are three types of CPs: negative Ir-Ir CPs, negative Si-Si CPs, and positive Ir-Si CPs. (b) The Ir-Si network in IrSi, overlaid on the average positions in gray, featuring trimers of Ir atoms separated by Ir monomers. In the red box is a single Ir monomer, while the blue boxes each surround a pair of monomers. Full purple lines represent Ir-Ir distances <3.12 Å, while full gold lines represent Si-Si distances <3.20 Å.

such Ir atoms as monomers. Each monomer acts on its neighboring Si bridges with positive CP, while negative CPs occur between the Si atoms. Motions of the Ir atoms will naturally drive changes in the Si-Si spacing. In particular, the Si-Si negative CPs running along the zig-zag chains are stretched when Ir atoms move apart.

These conflicts are evident when we consider the same network in the refined IrSi structure, where the modulations of the Ir atoms lead to chains of trimers separated by monomers which occur either individually or as pairs. In Figure 7b, we highlight the atomic arrangement of a trimer-monomer-trimer motif with a red box. The Ir monomer is formed when the neighboring Ir atoms move away from it to become the terminal atoms of the trimers to the left and right. The two bridging Si atoms around the monomer are pulled apart from both sides, leading to expanded homoatomic distances against the negative Si-Si CPs, an unfavorable arrangement. However, a pattern of alternating monomers and trimers would have an average of 1 additional Ir-Ir bond for each Ir, in accord with the 18−*n* rule.

The situation is different when two monomers appear adjacent to each other (shown in the blue boxes in Figure 7b). When two Ir monomers are placed side-by-side, the Ir atoms pull apart, leading to one long Ir-Ir contact and two of intermediate length; for instance, the leftmost blue box has Ir-Ir distances of 3.14 Å, 3.50 Å, and 3.28 Å. The bridging Si atom between them remains largely unmoved. However, the Si atoms on either side of the diverging Ir atoms are pushed in the same direction via the Ir-Si CPs, resulting in shorter Si-Si distances on the edges of this monomeric region (3.18 Å and 3.15 Å) and only one Si atom with expanded Si-Si distances on both sides. In contrast, the previous arrangement leaves two Si atoms in this unfortunate scenario. So while the repetition of monomers reduces the average number of Ir-Ir bonds per Ir atom slightly, it involves less stretching of the Si sublattice. The balance of these two effects likely underlies the incommensurability of this compound.

From this point of view, we can also see why trimers would be preferred to dimers. In the formation of trimers, certain Si-Si distances along *b* are decreased (yellow bars in Figure 7b), which would satisfy their negative CPs to some degree. In a dimerized structure, however, the Ir motions lead to balanced forces on each Si atom, so that no Si motion along *b* is allowed. No Si-Si CP relief is then attainable.

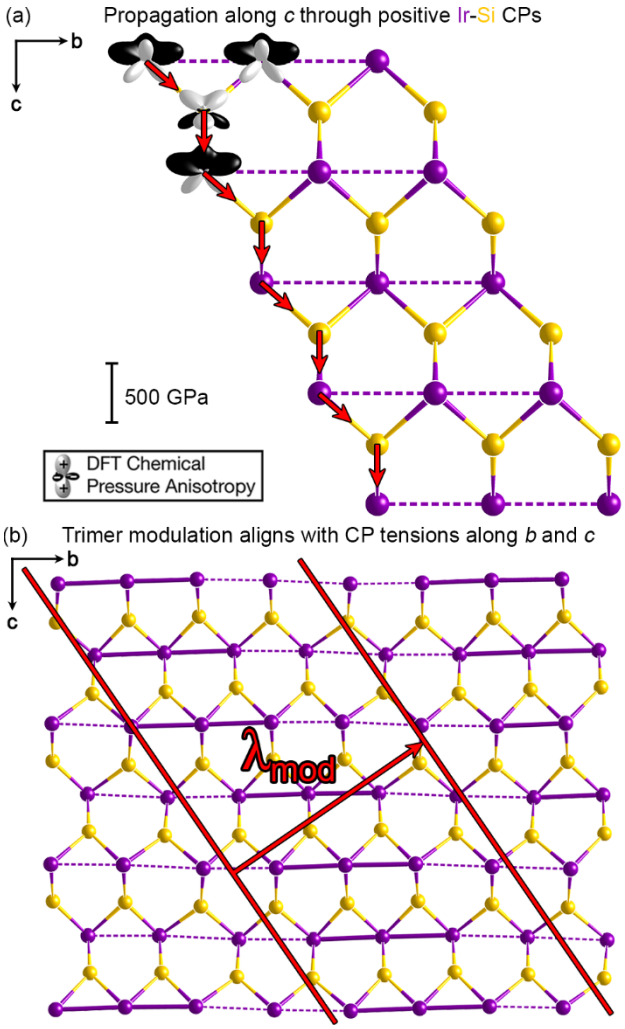

Figure 8. (a) The buckled honeycomb Ir-Si network in the *bc*-plane of the average structure. The pattern of Ir trimers and monomers propagates along *c* via the Ir-Si positive pressures. (b) The observed IrSi structure, overlaid with the direction and periodicity, λ_{mod}, of the modulation wave.

These considerations have allowed us to understand the *b* component of the modulation in IrSi. The distribution of Ir-Si CPs in a honeycomb-like network similarly provides a path for the propagation of the modulation along *c*. In Figure 8a, a slab of this Ir-Si network in the average structure is shown overlaid with its CP lobes shown for a single Si atom and its nearest Ir neighbors. By following the white lobes, we can see that the positive Ir-Si CPs trace zigzag paths that run diagonally across the plane (red arrows). Trimerization in one chain will naturally encourage a trimerization in chains above and below it, offset by half an average cell spacing along *b*. In Figure 8b, we test this idea by overlaying the modulation wave period (λ_{mod}, indicated with the red arrow) over the structure. The contours of constant phase (red lines) align roughly with the direction of positive CP propagation outlined in Figure 8a.

3.8. Schematic view of IrSi's modulated structure in terms of atomic packing and electronics. As we have seen above, the modulations in IrSi arrive from the close coordination of the electronic and atomic packing factors. These results can be summarized schematically with an abstract potential energy surface, as we show in Scheme 1. Here, we consider the advantages and disadvantages of different structural transitions away from the MnP-type parent structure as described by their valence electron counts and q_y, the wave vector of the modulations in the *y* coordinate of the Ir sublattice.

Scheme 1. Interpretation of IrSi's Structural Transition in Terms of the FAST Principle.

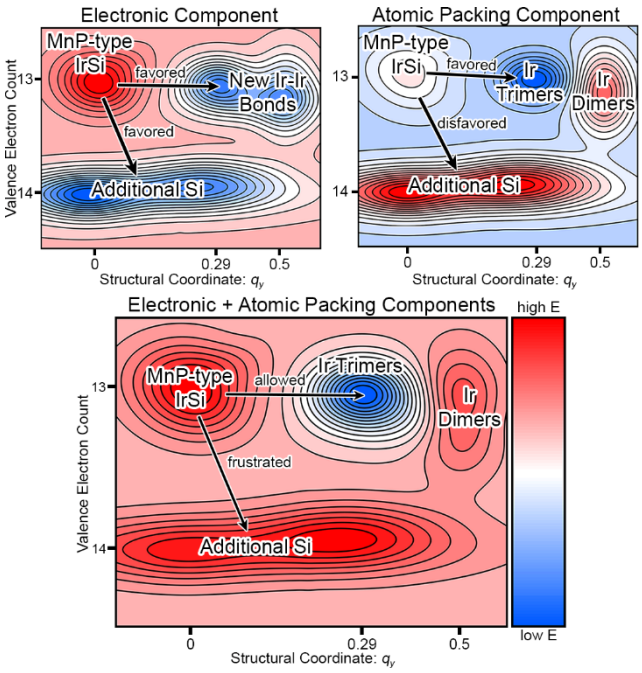

Let's begin with the electronic component of IrSi's structural landscape. The original MnP-type structure appears as a high-energy (red) peak at 13 electrons/Ir atom and $q_y = 0$, reflecting its electron-poor character when no modulation is included. There are multiple options available to solve the electron deficiency: forming more Ir-Ir bonds or adding Si. More Ir-Ir bonds requires only a change in q_y, placing these lower energy (blue) structural variations to the right of MnP-type IrSi. However, we include multiple local minima, as there is more than one bonding pattern that yields an average of $n = 5$ Ir-Ir bonds in the structure. For instance, $q_y = ½$ corresponds to dimers and $q_y < ½$ represents longer scale variations. On the other hand, the addition of Si atoms changes the valence electron count, moving this low-energy feature below the parent structure in the landscape. However, while valence electron count sets a Si content, it does not direct the distribution of Si atoms along *y*. We thus represent this feature along the full q_y range of the landscape.

If we instead move to the atomic packing factor's energy landscape, a very different story emerges. Here, the MnP-type structure is not as clearly disfavored, indicated by its light pink peak in the landscape, though there are opportunities to solve CP tensions via a structural transition (the Ir-Ir negative CPs, for instance). In this case, we can be a bit more specific about the energetic gain of changing q_y: forming trimers is a more favorable configuration than forming dimers (shown as a low energy area at shorter q_y and a high energy peak at longer q_y, respectively), with trimers winning out as a compromise between the structure's desire for regular contraction of the Ir sublattice against the backdrop of negative Si-Si CPs. We expect that additional Si atoms are also disfavored with respect to the atomic packing factor, as they would increase the number of Ir-Si contacts (positive CP) in the structure or require further expansion of the Ir sublattice (negative CP).

Summing the landscapes of both chemical factors gives the full structural landscape. In this case, the most favored transition is from MnP-type IrSi to the formation of Ir trimers along *y*, which sees the structure go from a high energy area (red) to a low energy area (blue). Taken together, we can use these schemes to see that the structural transition is driven by the low valence electron count of the MnP type and is guided to form trimers by the conflicting desire for contraction in the separate sublattices along negative CPs.

Such themes can be recognized in many other systems: IrSi joins a larger family of systems showing structural behavior dictated by the interaction of electronic and atomic packing factors. In all these cases—whether we consider incommensurate modulations in IrSi, the formation of incommensurate channels in the Nowotny Chimney Ladders,[14,23] or superstructure formation in $PtGa_2$[27]—complex structural phenomena are most favorable when the electronic and atomic packing factors work cooperatively, whereas they become constrained when the two factors clash, a trend that we might call the Frustrated and Allowed Structural Transitions (FAST) principle. Here, allowed structural phenomena are those that have favorable or neutral paths in both factors; we expect them to be relatively easy to experimentally realize. On the other hand, frustrated structural transitions are those where the factors disagree on the benefits of a structural transition and are expected to be more difficult to experimentally realize.

4. CONCLUSIONS

In this Article, we have investigated how the electronic and the atomic packing factors drive IrSi to adopt an incommensurately

modulated version of the MnP structure. We began with a theoretical investigation of MnP-type IrSi, where the parent structure is electron-poor relative to the ideal 18–*n* electron count, and the CP scheme revealed Si CP quadrupoles and negative CPs along the homoatomic contacts that could enable a structural response to these electron deficiencies. We then synthesized and structurally characterized IrSi, revealing its incommensurately modulated structure, the major features of which can be traced back to the tensions of the parent structure: an increase in Ir-Ir bonding and the uneven spacing of Ir trimers along *b* due to conflicting Ir-Ir and Si-Si negative CPs. The results of our investigation into IrSi's structural chemistry led us to propose the FAST principle.

It will be interesting to see how the FAST principle can be used to create similar maps to that of Scheme 1 for the navigation of new structural chemistry in other intermetallic systems. To begin with, we might investigate how other nominally MnP-type structures respond to electronic and atomic packing tensions in that parent structure; one interesting case might be RhSi, where polymorphism and two Si-rich distortions of the MnP-type structure are reported.[68,69] In addition, the FAST principle could be further developed by exploring the roles of atomic packing and electronics are reversed, with atomic size effects providing a driving force that is steered by electronic considerations.

ASSOCIATED CONTENT

Supporting Information. Crystallographic details for the average and (3+1)D structures of IrSi; powder X-ray diffraction results; energy-dispersive X-ray spectroscopy results; additional computational details; computationally optimized geometries; DFT-calibrated Hückel parameters used in this work; comparisons of DFT and best-fit Hückel DOS curves; comparisons of DOS with and without spin-orbit coupling; raMO analysis of MnP-type IrSi; CP schemes calculated with free-ion profiles constructed at different percentages of the Bader charge; comparison of the CP schemes with and without spin-orbit coupling; animation of Si motions in response to Ir sublattice contractions.

AUTHOR INFORMATION

Corresponding Author

*email: danny@chem.wisc.edu

ACKNOWLEDGMENT

The authors thank Dr. Katerina Hilleke for engaging discussions that led to the development of the FAST model, as well as the construction of the more general version of Scheme 1. HMW thanks the National Science Foundation for a graduate student fellowship (DGE-1747503). The authors also gratefully acknowledge the financial support of NSF Grant DMR-1809594. This work includes calculations that used computing resources supported by NSF Grant CHE-0840494. Use of the Advanced Photon Source at Argonne National Laboratory was supported by the U. S. Department of Energy, Office of Science, Office of Basic Energy Sciences, under Contract No. DE-AC02-06CH11357.

REFERENCES

(1) Hume-Rothery, W. The nature, properties and conditions of formation of intermetallic compounds with special reference to certain compounds of tin. I-V. *J. Inst. Met.* **1926**, *35*, 295-299.

(2) Hume-Rothery, W.; Raynor, G. V. *The Structure of Metals and Alloys*; 4th ed.; Institute of Metals: London, 1962.

(3) Mizutani, U. *The Hume-Rothery rules for structurally complex alloy phases*; World Scientific Publishing Co. Pte. Ltd., 2010; Vol. 3.

(4) Pettifor, D. G. Structure maps in magnetic alloy design. *Physica B+C* **1988**, *149*, 3-10.

(5) Villars, P. A three-dimensional structural stability diagram for 998 binary AB intermetallic compounds. *J. Less Common Met.* **1983**, *92*, 215-238.

(6) Villars, P. *Pearson's handbook of crystallographic data for intermetallic phases*; 2nd ed.; ASM International: Materials Park, OH :, 1991.

(7) Raju, S.; Mohandas, E.; Raghunathan, V. S. A study of ternary element site substitution in Ni_3Al using pseudopotential orbital radii based structure maps. *Scripta Mater.* **1996**, *34*, 1785-1790.

(8) Guénée, L.; Yvon, K. Structure stability maps for intermetallic AB_5 compounds. *J. Alloys Compd.* **2003**, *356–357*, 114-119.

(9) Tkachuk, A. V.; Mar, A. Electron-poor $SrAu_xIn_{4-x}$ ($0.5 \le x \le 1.2$) and $SrAu_xSn_{4-x}$ ($1.3 \le x \le 2.2$) phases with the $BaAl_4$-type structure. *J. Solid State Chem.* **2007**, *180*, 2298-2304.

(10) Xia, S.; Bobev, S. Interplay between Size and Electronic Effects in Determining the Homogeneity Range of the $A_9Zn_{4+x}Pn_9$ and $A_9Cd_{4+x}Pn_9$ Phases ($0 \le x \le 0.5$), A = Ca, Sr, Yb, Eu; Pn = Sb, Bi. *J. Am. Chem. Soc.* **2007**, *129*, 10011-10018.

(11) Amerioun, S.; Häussermann, U. Structure and Bonding of Sr_3In_{11}: How Size and Electronic Effects Determine Structural Stability of Polar Intermetallic Compounds. *Inorg. Chem.* **2003**, *42*, 7782-7788.

(12) Zintl, E. Intermetallische Verbindungen. *Angew. Chem.* **1939**, *52*, 1-6.

(13) Nesper, R. The Zintl-Klemm Concept – A Historical Survey. *Z. Anorg. Allg. Chem.* **2014**, *640*, 2639-2648.

(14) Yannello, V. J.; Fredrickson, D. C. Orbital Origins of Helices and Magic Electron Counts in the Nowotny Chimney Ladders: the 18 – *n* Rule and a Path to Incommensurability. *Inorg. Chem.* **2014**, *53*, 10627-10631.

(15) Yannello, V. J.; Fredrickson, D. C. Generality of the 18 – *n* Rule: Intermetallic Structural Chemistry Explained through Isolobal Analogies to Transition Metal Complexes. *Inorg. Chem.* **2015**, *54*, 11385-11398.

(16) Berns, V. M.; Engelkemier, J.; Guo, Y.; Kilduff, B. J.; Fredrickson, D. C. Progress in Visualizing Atomic Size Effects with DFT-Chemical Pressure Analysis: From Isolated Atoms to Trends in AB_5 Intermetallics. *J. Chem. Theory Comput.* **2014**, *10*, 3380-3392.

(17) Engelkemier, J.; Berns, V. M.; Fredrickson, D. C. First-Principles Elucidation of Atomic Size Effects Using DFT-Chemical Pressure Analysis: Origins of $Ca_{36}Sn_{23}$'s Long-Period Superstructure. *J. Chem. Theory Comput.* **2013**, *9*, 3170-3180.

(18) Fredrickson, D. C. DFT-Chemical Pressure Analysis: Visualizing the Role of Atomic Size in Shaping the Structures of Inorganic Materials. *J. Am. Chem. Soc.* **2012**, *134*, 5991-5999.

(19) Hilleke, K. P.; Fredrickson, D. C. Discerning Chemical Pressure amidst Weak Potentials: Vibrational Modes and Dumbbell/Atom Substitution in Intermetallic Aluminides. *J. Phys. Chem. A* **2018**, *122*, 8412-8426.

(20) Jeitschko, W.; Parthé, E. The crystal structure of $Rh_{17}Ga_{22}$, an example of a new kind of electron compound. *Acta Crystallogr.* **1967**, *22*, 417-430.
(21) Pearson, W. Phases with Nowotny chimney-ladder structures considered as `electron' phases. *Acta Crystallogr. B* **1970**, *26*, 1044-1046.
(22) Fredrickson, D. C.; Lee, S.; Hoffmann, R.; Lin, J. The Nowotny Chimney Ladder Phases: Following the cpseudo Clue toward an Explanation of the 14 Electron Rule. *Inorg. Chem.* **2004**, *43*, 6151-6158.
(23) Lu, E.; Fredrickson, D. C. Templating Structural Progessions in Intermetallics: How Chemical Pressure Directs Helix Formation in the Nowotny Chimney Ladders. *Inorg. Chem.* **2019**, *58*, 4063-4066.
(24) Vinokur, A. I.; Hilleke, K. P.; Fredrickson, D. C. Principles of weakly ordered domains in intermetallics: the cooperative effects of atomic packing and electronics in Fe_2Al_5. *Acta Crystallogr. A* **2019**, *75*, 297-306.
(25) Zintl, E.; Harder, A.; Haucke, W. Legierungsphasen mit Fluoritstruktur. *Z. Phys. Chem.* **1937**, *35B*, 354.
(26) Swenson, D.; Morosin, B. On the preparation and crystal structure of a new form of $PtGa_2$. *J. Alloys Compd.* **1996**, *243*, 173-181.
(27) Mitchell Warden, H. E.; Voyles, P. M.; Fredrickson, D. C. Paths to Stabilizing Electronically Aberrant Compounds: A Defect-Stabilized Polymorph and Constrained Atomic Motion in $PtGa_2$. *Inorg. Chem.* **2018**, *57*, 13880-13894.
(28) Yannello, V. J.; Kilduff, B. J.; Fredrickson, D. C. Isolobal Analogies in Intermetallics: The Reversed Approximation MO Approach and Applications to $CrGa_4$- and Ir_3Ge_7-Type Phases. *Inorg. Chem.* **2014**, *53*, 2730-2741.
(29) Kresse, G.; Hafner, J. Ab initio molecular dynamics for liquid metals. *Phys. Rev. B* **1993**, *47*, 558.
(30) Kresse, G.; Hafner, J. Ab initio molecular-dynamics simulation of the liquid-metal—amorphous-semiconductor transition in germanium. *Phys. Rev. B* **1994**, *49*, 14251-14269.
(31) Kresse, G.; Furthmüller, J. Efficient iterative schemes for ab initio total-energy calculations using a plane-wave basis set. *Phys. Rev. B* **1996**, *54*, 11169-11186.
(32) Kresse, G.; Furthmüller, J. Efficiency of ab-initio total energy calculations for metals and semiconductors using a plane-wave basis set. *Comput. Mater. Sci* **1996**, *6*, 15-50.
(33) Perdew, J. P.; Chevary, J. A.; Vosko, S. H.; Jackson, K. A.; Pederson, M. R.; Singh, D. J.; Fiolhais, C. Atoms, molecules, solids, and surfaces: Applications of the generalized gradient approximation for exchange and correlation. *Phys. Rev. B* **1992**, *46*, 6671-6687.
(34) Perdew, J. P.; Chevary, J. A.; Vosko, S. H.; Jackson, K. A.; Pederson, M. R.; Singh, D. J.; Fiolhais, C. Erratum: Atoms, molecules, solids, and surfaces: Applications of the generalized gradient approximation for exchange and correlation. *Phys. Rev. B* **1993**, *48*, 4978-4978.
(35) Perdew, J. P.; Burke, K.; Ernzerhof, M. Generalized Gradient Approximation Made Simple. *Phys. Rev. Lett.* **1996**, *77*, 3865-3868.
(36) Perdew, J. P.; Burke, K.; Ernzerhof, M. Generalized Gradient Approximation Made Simple [Phys. Rev. Lett. 77, 3865 (1996)]. *Phys. Rev. Lett.* **1997**, *78*, 1396-1396.
(37) Blöchl, P. E. Projector augmented-wave method. *Phys. Rev. B* **1994**, *50*, 17953.
(38) Kresse, G.; Joubert, D. From ultrasoft pseudopotentials to the projector augmented-wave method. *Phys. Rev. B* **1999**, *59*, 1758-1775.
(39) Stacey, T. E.; Fredrickson, D. C. Perceiving Molecular Themes in the Structures and Bonding of Intermetallic Phases: The Role of Hückel Theory in an *ab initio* Era. *Dalton Trans.* **2012**, *41*, 7801-7813.
(40) Landrum, G. A. G., W. V. YAeHMOP: Yet Another Extended Hückel Molecular Orbital Package, YAeHMOP is freely available via the Internet at URL: https://sourceforge.net/projects/yaehmop/.
(41) Vanderbilt, D. Soft Self-consistent Pseudopotentials in a Generalized Eigenvalue Formalism. *Phys. Rev. B* **1990**, *41*, 7892-7895.
(42) Gonze, X.; Beuken, J. M.; Caracas, R.; Detraux, F.; Fuchs, M.; Rignanese, G. M.; Sindic, L.; Verstraete, M.; Zerah, G.; Jollet, F.; Torrent, M.; Roy, A.; Mikami, M.; Ghosez, P.; Raty, J. Y.; Allan, D. C. First-principles computation of material properties: the ABINIT software project. *Comput. Mater. Sci* **2002**, *25*, 478-492.
(43) Gonze, X. A brief introduction to the ABINIT software package. *Z. Kristallog. – Cryst. Mater.* **2005**, *220*, 558.
(44) Gonze, X.; Amadon, B.; Anglade, P. M.; Beuken, J. M.; Bottin, F.; Boulanger, P.; Bruneval, F.; Caliste, D.; Caracas, R.; Côté, M.; Deutsch, T.; Genovese, L.; Ghosez, P.; Giantomassi, M.; Goedecker, S.; Hamann, D. R.; Hermet, P.; Jollet, F.; Jomard, G.; Leroux, S.; Mancini, M.; Mazevet, S.; Oliveira, M. J. T.; Onida, G.; Pouillon, Y.; Rangel, T.; Rignanese, G. M.; Sangalli, D.; Shaltaf, R.; Torrent, M.; Verstraete, M. J.; Zerah, G.; Zwanziger, J. W. ABINIT: First-principles approach to material and nanosystem properties. *Comput. Phys. Commun.* **2009**, *180*, 2582-2615.
(45) Hartwigsen, C.; Goedecker, S.; Hutter, J. Relativistic separable dual-space Gaussian pseudopotentials from H to Rn. *Phys. Rev. B* **1998**, *58*, 3641-3662.
(46) Bader, R. F. W. *Atoms in molecules: a quantum theory*; Oxford; New York: Clarendon Press, 1990.
(47) Henkelman, G.; Arnaldsson, A.; Jónsson, H. A fast and robust algorithm for Bader decomposition of charge density. *Comput. Mater. Sci* **2006**, *36*, 354-360.
(48) Sanville, E.; Kenny Steven, D.; Smith, R.; Henkelman, G. Improved grid-based algorithm for Bader charge allocation. *J. Comput. Chem.* **2007**, *28*, 899-908.
(49) Tang, W.; Sanville, E.; Henkelman, G. A grid-based Bader analysis algorithm without lattice bias. *J. Phys.: Condens. Matter* **2009**, *21*, 084204.
(50) Oliveira, M. J. T.; Nogueira, F. Generating relativistic pseudo-potentials with explicit incorporation of semi-core states using APE, the Atomic Pseudo-potentials Engine. *Comput. Phys. Commun.* **2008**, *178*, 524-534.
(51) Kandpal, H. C.; Felser, C.; Seshadri, R. Covalent bonding and the nature of band gaps in some half-Heusler compounds. *J. Phys. D: Appl. Phys.* **2006**, *39*, 776-785.
(52) Oszlányi, G.; Sütő, A. Ab initio structure solution by charge flipping. *Acta Crystallogr. A* **2004**, *60*, 134-141.
(53) Oszlányi, G.; Sütő, A. Ab initio structure solution by charge flipping. II. Use of weak reflections. *Acta Crystallogr. A* **2005**, *61*, 147-152.
(54) Palatinus, L.; Chapuis, G. SUPERFLIP - a computer program for the solution of crystal structures by charge flipping in arbitrary dimensions. *J. Appl. Crystallogr.* **2007**, *40*, 786-790.
(55) Petříček, V.; Dušek, M.; Palatinus, L. Crystallographic Computing System JANA2006: General features. *Z. Kristallog. – Cryst. Mater.* **2014**, *229*, 345-352.
(56) MnP is actually 5 electrons/Mn short of the 18-*n* expectation. It is probably better understood in terms of an ionic or Zintl-like electron counting scheme. This appears to be an example of a single structure type being adopted by compounds with different bonding schemes, c.f. CsCl and CoAl.

(57) Engelkemier, J.; Fredrickson, D. C. Chemical Pressure Schemes for the Prediction of Soft Phonon Modes: A Chemist's Guide to the Vibrations of Solid State Materials. *Chem. Mater.* **2016**, *28*, 3171-3183.
(58) Kilduff, B. J.; Fredrickson, D. C. Chemical Pressure-Driven Incommensurability in $CaPd_5$: Clues to High-Pressure Chemistry Offered by Complex Intermetallics. *Inorg. Chem.* **2016**, *55*, 6781-6793.
(59) Korst, W. L.; Finnie, L. N.; Searcy, A. W. The Crystal Structures of the Monosilicides of Osmium, Iridium and Ruthenium. *J. Phys. Chem.* **1957**, *61*, 1541-1543.
(60) Engström, I.; Zackrisson, F. X-Ray Studies of Silicon-rich Iridium Silicides. *Acta Chem. Scand.* **1970**, *24*, 2109-2116.
(61) Allevato, C. E.; Vining, C. B. Phase diagram and electrical behavior of silicon-rich iridium silicide compounds. *J. Alloys Compd.* **1993**, *200*, 99-105.
(62) Göransson, K.; Engström, I.; Noläng, B. Structure refinements for some platinum metal monosilicides. *J. Alloys Compd.* **1995**, *219*, 107-110.
(63) de Wolff, P. M. The Pseudo-Symmetry of Modulated Crystal Structures. *Acta Crystallogr. A* **1974**, *30*, 777-785.
(64) Bergerhoff, G.; Hundt, R.; Sievers, R.; Brown, I. D. The Inorganic Crystal Structure Data Base. *J. Chem. Inf. Comput. Sci.* **1983**, *23*, 66-69.
(65) Bergerhoff, G.; Brown, I. D. Inorganic Crystal Structure Database In *Crystallographic Databases*; Allen, F. H., Bergerhoff, Sievers, R., Eds.; International Union of Crystallography: Chester, 1987, p 77-95.
(66) Unfortunately, the off-axis orientation of the modulations and the large number of repeats required to fully capture the trimer/monomer pattern of IrSi's structure make doing calculations on a realistic periodic approximant prohibitive.
(67) Lidin, S.; Folkers, L. Y_3Ru_{2-x}—A Representative of a Composite Modulated Family of Intermetallics. *Crystals* **2019**, *9*, 189.
(68) Engström, I. The Crystal Strucutre of Rh_4Si_5 and its Relation to Other Members of the MnP Structure Family. *Acta Chem. Scand.* **1968**, *22*, 3127-3136.
(69) Engström, I.; Persson, E. The Crystal Structure of Rh_3Si_4. *Acta Chem. Scand.* **1968**, *22*, 3120-3126.

For Table of Contents Use Only